

Coulomb, Landau and Maximally Abelian Gauge Fixing in Lattice QCD with Multi-GPUs

Mario Schröck^{a,*}, Hannes Vogt^{b,**}

^a*Institut für Physik, FB Theoretische Physik, Universität Graz, 8010 Graz, Austria*

^b*Institut für Theoretische Physik, Auf der Morgenstelle 14, 72076 Tübingen, Germany*

Abstract

A lattice gauge theory framework for simulations on graphic processing units (GPUs) using NVIDIA's CUDA is presented. The code comprises template classes that take care of an optimal data pattern to ensure coalesced reading from device memory to achieve maximum performance. In this work we concentrate on applications for lattice gauge fixing in 3+1 dimensional SU(3) lattice gauge field theories. We employ the overrelaxation, stochastic relaxation and simulated annealing algorithms which are perfectly suited to be accelerated by highly parallel architectures like GPUs. The applications support the Coulomb, Landau and maximally Abelian gauges. Moreover, we explore the evolution of the numerical accuracy of the SU(3) valued degrees of freedom over the runtime of the algorithms in single (SP) and double precision (DP). Therefrom we draw conclusions on the reliability of SP and DP simulations and suggest a mixed precision scheme that performs the critical parts of the algorithm in full DP while retaining 80–90% of the SP performance. Finally, multi-GPUs are adopted to overcome the memory constraint of single GPUs. A communicator class which hides the MPI data exchange at the boundaries of the lattice domains, via the low bandwidth PCI-Bus, effectively behind calculations in the inner part of the domain is presented. Linear scaling using 16 NVIDIA Tesla C2070 devices and a maximum performance of 3.5 Teraflops on lattices of size down to $64^3 \times 256$ is demonstrated.

Keywords: Lattice QCD, Maximally Abelian, Gauge fixing, Overrelaxation, Simulated annealing, GPU, CUDA

**E-mail address:* mario.schroeck@uni-graz.at

***E-mail address:* hannes.vogt@uni-tuebingen.de

1. Introduction

Quantum Chromodynamics (QCD) is nowadays, 40 years after its birth, widely accepted as the correct theory of the strong nuclear force which binds the protons and neutrons in the cores of atoms. The guiding principle in the construction of QCD was the local gauge symmetry which has led before to the very successful theory of quantum electrodynamics (QED) that describes the interactions of electrons and light. Local gauge symmetry is the freedom to perform a transformation of the vector fields of the theory, independently at each point of space-time, without changing the physics the theory describes.

Lattice QCD which lives on a discretized space-time background opposed to the continuous world of the original theory, offers a formulation of the gauge theory that is well suited to be simulated on a computer and hence can be used to test the theory against experiment. Furthermore, lattice simulations can help to gain insights in the highly nontrivial, nonperturbative regime of the interactions between quarks and gluons which are the degrees of freedom of QCD.

The gauge symmetry, given below in its discrete version, states that physical observables will remain unchanged if a local transformation of the form

$$g(x)U_\mu(x)g(x + \hat{\mu})^\dagger \tag{1}$$

is being carried out. Here, the gauge fields or *link variables* $U_\mu(x)$ as well as the gauge transformations $g(x)$ are elements of the underlying gauge group which is $SU(3)$ in the case of QCD. The index $\mu = 0, \dots, 3$ refers to the direction in four dimensional space-time and with $x + \hat{\mu}$ we denote the neighbor lattice site of x in the μ -direction. The link variables of lattice QCD are connected to the algebra valued continuum gauge fields $A_\mu(x)$ via

$$U_\mu(x) = e^{iagA_\mu(x)}. \tag{2}$$

Whereas physical observables that can be measured in experiments must be independent of the gauge, fixing the gauge, i.e., choosing a particular gauge transformation $g(x)$ for all x , is essential when, e.g., studying gauge dependent quantities like the fundamental two point functions of the theory.

As a typical example of a gauge condition that may be enforced at all space-time points x , we consider the manifestly covariant Landau gauge

$$\partial_\mu A_\mu(x) = 0, \tag{3}$$

here stated in the language of continuum field theories. As we will discuss in the next Section, the continuum gauge condition Eq. (3) translates to a large scale optimization problem in lattice QCD with $\mathcal{O}(VN_c^2)$ degrees of freedom where $V = N_s^3 \times N_t$ is the 3+1 dimensional lattice volume. Consequently, the process of fixing the gauge on the lattice demands a major part of the whole simulation's computer time and the possible acceleration by highly parallel hardware architectures like graphic processing units (GPUs) will be of great practical use.

A more conceptual issue of gauge fixing is that the set of gauge transformations $g(x)$ that fulfill a desired gauge condition is far from being unique. The set of gauge equivalent configurations of a given gauge field is called the gauge orbit. The gauge fixing condition can be depicted as a hypersurface living in the space of all gauge fields. Each of the multiple intersections of the gauge orbit with the gauge fixing hypersurface is called a Gribov copy.

Gribov copies play a crucial role in restoring the BRST symmetry on the lattice: fixing a gauge via the Faddeev–Popov procedure on the lattice for a compact group boils down to inserting the sum over signs of the corresponding Faddeev–Popov determinants evaluated at all the Gribov copies. Neuberger [1] showed that the sum for any covariant gauge turns out to be zero for any standard model gauge group, $SU(N)$, and for compact $U(1)$, making the expectation value of a gauge-fixed observable $0/0$. The zero comes up because each Gribov copy comes in pairs with opposite sign of the Faddeev–Popov determinant. This in turn makes it impossible to construct a BRST symmetry on the lattice. This is called the Neuberger $0/0$ problem. Following a topological interpretation of the Neuberger $0/0$ problem, in Refs. [2, 3] a modified lattice Landau gauge was proposed which evaded the problem. There, because the Faddeev–Popov is shown to be strictly positive (semi-)definite, the cancellation is avoided. However, it is yet to be shown that the number of Gribov copies in the modified lattice Landau gauge is independent of the background gauge field. Interestingly, recently, a deep relation between lattice gauge fixing and lattice supersymmetry has been proposed in Ref. [4, 5]: the partition functions of a class of supersymmetric Yang–Mills theories can be viewed as a gauge fixing partition function à la

Faddeev–Popov and the “Gribov copies” are then nothing but the classical configurations of the theory.

A possible way out of the problem of the existence of Gribov copies is to restrict the gauge fixing hypersurface to a region which the gauge orbit intersects only once. An example thereof is the so-called Fundamental Modular Region [6] which contains only that intersection of the gauge orbit which corresponds to the global optimum of the gauge condition. Unfortunately, no algorithm is known which finds the global optimum of the gauge condition within finite simulation time. *Simulated annealing*, however, has been shown to highly favor optima closer to the global optimum [7, 8] and moreover it can be shown that, in the limit of infinite time, simulated annealing actually converges to the global maximum.

Recently, the problem of counting Gribov copies has gained a renewed interest. In Refs. [9], an explicit formula of the number of Gribov copies for any number of lattice sites is analytically derived for lattice Landau gauge for the one-dimensional compact $U(1)$ case. In Refs. [10, 11], a novel method based on Algebraic Geometry [12, 13, 14], which can count all the Gribov copies, was proposed. Although the method has only been able to work for small lattices, it is the only known method which guarantees to find all Gribov copies and hence it can work as a benchmark for other methods. One such alternative method is plain brute force, i.e., running a standard optimization algorithm over and over again from different starting points on the gauge orbit and collecting the results consecutively. Clearly, a high performance lattice gauge fixing code is essential for this task and since here one primarily focuses on small lattices, GPUs are favorable given the fact that CPU parallelization techniques are very limited for lattices of small extent.

In this work we present a set of applications for lattice gauge fixing based on the family of relaxation algorithms and simulated annealing. The applications are based on the CUDA accelerated Lattice–Graz–Tübingen code¹ that is written in CUDA C/C++ and makes heavy use of template classes in order to facilitate the extension to a broad variety of applications. Besides the standard relaxation algorithm [15], we support overrelaxation [16] and stochastic relaxation [17] to overcome the problem of critical slowing down. Moreover, the simulated annealing algorithm [7] with a heatbath kernel and microcanonical updates which increases the probability to reach the Funda-

¹Available for download at www.cuLGT.com

mental Modular Region has been implemented and tested. The code can be used to fix gauge configurations to the covariant Landau gauge $\partial_\mu A_\mu = 0$, $\mu = 0, \dots, 3$, the Coulomb gauge $\partial_i A_i = 0$, $i = 1, 2, 3$ and the maximally Abelian gauge.

Previous utilizations of GPUs in the field of lattice QCD mainly focused on solvers of linear systems [18, 21]

A first attempt of porting lattice gauge fixing with the overrelaxation algorithm to the GPU has been reported in [26, 27]. An alternative approach based on the steepest descent method has been presented in [28]. For a more general discussion of lattice gauge fixing and its problems we refer the reader to [29].

The remainder of this work is organized as follows: in Sec. 2 the optimization problem is stated and the algorithms of choice are presented. In Sec. 3 we summarize some hardware properties of the NVIDIA GPUs that we use for our investigation and moreover briefly discuss NVIDIA's programming environment *CUDA*. Next, in Sec. 4, we give details of our implementation and the cuLGT framework and moreover discuss numerical accuracy issues. To overcome the memory constraint of single GPUs we extend our implementation to support multi-GPUs; all details thereto are presented in Sec. 5. Finally, in Sec. 6 we show various performance results for single and multiple GPUs and furthermore present some convergence results of the algorithms. In Sec. 7 we summarize and conclude.

2. The algorithms

In this Section we will first summarize the defining equations of the optimization problem. Subsequently, we discuss the various flavors of the update kernels and finally we list the main underlying algorithm of this work explicitly in terms of pseudo-code.

2.1. The gauge functionals

On the lattice, enforcing a gauge condition, e.g., Eq. (3) is equivalent to maximizing the corresponding gauge functional. We support three different kinds of gauge conditions and here we give the related gauge functionals and moreover a measure of the iteratively achieved gauge quality that can serve as a stopping criterion for the algorithm.

2.1.1. Coulomb and Landau gauge

The continuum Landau gauge condition, Eq. (3), is fulfilled if and only if the lattice gauge functional

$$F_{\text{Landau}}^g[U] = \frac{1}{N_c N_d V} \Re \sum_{\mu, x} \text{tr} [U_\mu^g(x)], \quad (4)$$

resides in a stationary point with respect to gauge transformations $g(x) \in \text{SU}(N_c)$. In the above equation we made use of the short hand notation

$$U_\mu^g(x) \equiv g(x) U_\mu(x) g(x + \hat{\mu})^\dagger. \quad (5)$$

Furthermore, with N_c we denote the dimension of the gauge group $\text{SU}(N_c)$, $N_c = 3$ for QCD, N_d is the number of space-time dimensions, ($N_d = 4$ for our work) and V is the number of lattice points. When switching to Coulomb gauge, all that changes is that the sum in Eq. (4) becomes limited to the spatial components of the Dirac index μ , thus leaving out the temporal one. Consequently, the optimization of Eq. (4) for Coulomb gauge can be performed independently on different time-slices.

A measure θ of how well the Landau/Coulomb gauge condition is satisfied on a given gauge field configuration is the average L_2 -norm of the gauge fixing violation $\Delta(x)$, i.e., the discrete derivative of the continuum gauge fields

$$\Delta(x) \equiv \sum_{\mu} (A_\mu(x) - A_\mu(x - \hat{\mu})) = 0, \quad (6)$$

$$\theta \equiv \frac{1}{N_c V} \sum_x \text{tr} [\Delta(x) \Delta(x)^\dagger]. \quad (7)$$

2.1.2. Maximally Abelian gauge

The gauge functional for the maximally Abelian gauge is, in the case of $\text{SU}(2)$, given by

$$F_{\text{MAG2}}^g[U] = \frac{1}{2N_d V} \sum_{x, \mu} \text{tr} [\sigma_3 U_\mu(x) \sigma_3 U_\mu(x)^\dagger] \quad (8)$$

where σ_3 is the diagonal matrix of the three Pauli matrices that correspond to the generators of $\text{SU}(2)$. Equivalently, in the case of $\text{SU}(3)$ the gauge functional reads

$$F_{\text{MAG3}}^g[U] = \frac{1}{3N_d V} \sum_{x, \mu} \text{tr} [\lambda_3 U_\mu(x) \lambda_3 U_\mu(x)^\dagger] + \text{tr} [\lambda_8 U_\mu(x) \lambda_8 U_\mu(x)^\dagger] \quad (9)$$

where λ_3 and λ_8 build the Cartan subalgebra of SU(3). Maximizing Eq. (9) is equivalent to minimizing the off-diagonal components $A_\mu^{(i)}(x)$, $i \neq 3, 8$ of the continuum gauge fields

$$A_\mu(x) = \frac{1}{2} \sum_{i=1}^8 \lambda_i A_\mu^{(i)}(x). \quad (10)$$

Note that maximizing Eq. (8) or Eq. (9), respectively, is equivalent to maximizing the squares of the diagonal of each gauge link

$$F_{\text{MAG}}^g[U] = \frac{1}{N_c N_d V} \sum_{x,\mu,i} |(U_\mu(x))_{ii}|^2 \quad (11)$$

which is the gauge functional that we use in practice.

When the SU(2) gauge functional Eq. (8) is stationary with respect to gauge transformations, then the off-diagonal elements of

$$X(x) = \sum_{\mu} (U_\mu(x) \sigma_3 U_\mu(x)^\dagger + U_\mu(x - \hat{\mu})^\dagger \sigma_3 U_\mu(x - \hat{\mu})) \quad (12)$$

must vanish [30]. Thus, for SU(2) we can use

$$\theta = \frac{1}{N_c V} \sum_x |(X(x))_{12}|^2 \quad (13)$$

as a measure of the gauge quality. The off-diagonal element $(X(x))_{12}$ reads explicitly

$$\begin{aligned} (X(x))_{12} = & \sum_{\mu} 2(u_{\mu,0}(x)u_{\mu,2}(x) + u_{\mu,1}(x)u_{\mu,3}(x) \\ & - iu_{\mu,0}(x)u_{\mu,1}(x) - iu_{\mu,2}(x)u_{\mu,3}(x) \\ & + u_{\mu,0}(x - \hat{\mu})u_{\mu,2}(x - \hat{\mu}) + u_{\mu,1}(x - \hat{\mu})u_{\mu,3}(x - \hat{\mu}) \\ & + iu_{\mu,0}(x - \hat{\mu})u_{\mu,1}(x - \hat{\mu}) - iu_{\mu,2}(x - \hat{\mu})u_{\mu,3}(x - \hat{\mu})) \end{aligned} \quad (14)$$

where we adopted the Cayley–Klein parametrization

$$U_\mu = \begin{pmatrix} u_{\mu,0} + iu_{\mu,3} & u_{\mu,2} + iu_{\mu,1} \\ -u_{\mu,2} + iu_{\mu,1} & u_{\mu,0} - iu_{\mu,3} \end{pmatrix}. \quad (15)$$

For SU(3), we use equivalently

$$\theta = \frac{1}{N_c V} \sum_x |(X(x))_{12} + (Y(x))_{12} + (Z(x))_{12}|^2 \quad (16)$$

where the matrices $X(x), Y(x), Z(x) \in \text{SU}(2)$ stem from the three SU(2) subgroups of SU(3).

2.2. Relaxation

Now that we stated the optimization problem, we can proceed with presenting the algorithms which we will use to find a solution to the problem before we will discuss the implementation with CUDA in the next Section.

The main idea of the relaxation algorithm is to sweep over the lattice site by site while optimizing the gauge functional locally. Thereby, as we will see below, can all sites of one of the two *parity subsets* (think of a checker board decomposition) be optimized at the same time since the newly generated local optimum is a function of the nearest neighbors only.

In the following we will discuss the calculation of the local optimum separately for Coulomb/Landau gauge and the maximally Abelian gauge.

2.2.1. Coulomb and Landau gauge

Instead of taking the complete global gauge functional into account,

$$F_{\text{Landau}}^g[U] = \frac{1}{2N_c N_d V} \Re \sum_x f_{\text{Landau}}^g(x), \quad (17)$$

the relaxation algorithm aims at optimizing the value of $F^g[U]$ locally, i.e., for all x the maximum of

$$f_{\text{Landau}}^g(x) = \Re \text{tr} [g(x)K(x)] \quad (18)$$

is sought. Here we introduced

$$K(x) := \sum_{\mu} \left(U_{\mu}(x)g(x + \hat{\mu})^{\dagger} + U_{\mu}(x - \hat{\mu})^{\dagger}g(x - \hat{\mu})^{\dagger} \right) \quad (19)$$

where the sum runs over all space-time indices for Landau gauge and for Coulomb gauge it leaves out the temporal index. The local maximum thereof is, in the case of the gauge group SU(2), simply given by

$$g(x) = K(x)^{\dagger} / \sqrt{\det K(x)^{\dagger}}. \quad (20)$$

For the gauge group SU(3) (QCD) one iteratively operates in the three SU(2) subgroups [31] and thereby optimizes the local SU(3) gauge functional.

2.2.2. Maximally Abelian gauge

Similarly as for the Coulomb and Landau gauges, the goal is to maximize the gauge functional Eq. (8) locally. Again, we only need to know how to achieve this for SU(2) and then we can operate in the SU(2) subgroups of SU(3) for applications in QCD.

Thus, for a given site x we want to maximize

$$f_{\text{MAG2}}^g(x) = \sum_{\mu} \text{tr} [\sigma_3 g(x) U_{\mu}(x) \sigma_3 U_{\mu}(x)^{\dagger} g(x)^{\dagger} + \sigma_3 U_{\mu}(x - \hat{\mu})^{\dagger} g(x) \sigma_3 g(x)^{\dagger} U_{\mu}(x - \hat{\mu})]. \quad (21)$$

Let us focus on the part of Eq. (21) with the up-going links only, i.e., the first term in the sum; the second term of Eq. (21) can be treated equivalently.

For the following discussion it will be useful to switch to the Cayley–Klein parametrization of $g(x)$ and $U_{\mu}(x)$,

$$g = g_0 \mathbf{1} + i \sum_{i=1}^3 g_i \sigma_i = \begin{pmatrix} g_0 + i g_3 & g_2 + i g_1 \\ -g_2 + i g_1 & g_0 - i g_3 \end{pmatrix} \quad (22)$$

and

$$U_{\mu} = \begin{pmatrix} u_{\mu,0} + i u_{\mu,3} & u_{\mu,2} + i u_{\mu,1} \\ -u_{\mu,2} + i u_{\mu,1} & u_{\mu,0} - i u_{\mu,3} \end{pmatrix}, \quad (23)$$

respectively, where for a simpler notation we suppressed the space-time argument x .

Taking the fact that transformations proportional to σ_3 leave the functional Eq. (8) unchanged into account (thus setting $g_3 = 0$) one obtains

$$f_{\text{MAG2}}^{\text{up}}(x) = \sum_{\mu} -2 \left(4g_0(g_1 u_{\mu,0} u_{\mu,1} + g_2 u_{\mu,0} u_{\mu,2} - g_2 u_{\mu,1} u_{\mu,3} + g_1 u_{\mu,2} u_{\mu,3}) + g_0^2 (-u_{\mu,0}^2 + u_{\mu,1}^2 + u_{\mu,2}^2 - u_{\mu,3}^2) + (g_1^2 + g_2^2) (u_{\mu,0}^2 - u_{\mu,1}^2 - u_{\mu,2}^2 + u_{\mu,3}^2) \right). \quad (24)$$

Using a matrix/vector notation with $\mathbf{g}^T \equiv (g_0, g_1, g_2)^T$ the latter can be written as

$$f_{\text{MAG2}}^{\text{up}}(x) = 2\mathbf{g}^T \begin{pmatrix} D & E & F \\ E & -D & 0 \\ F & 0 & -D \end{pmatrix} \mathbf{g} \quad (25)$$

where we defined

$$D = \sum_{\mu} \left(u_{\mu,0}^2 + u_{\mu,3}^2 - \frac{1}{2} \right) \quad (26)$$

$$E = 2 \sum_{\mu} (-u_{\mu,0}u_{\mu,1} - u_{\mu,2}u_{\mu,3}) \quad (27)$$

$$F = 2 \sum_{\mu} (-u_{\mu,0}u_{\mu,2} + u_{\mu,1}u_{\mu,3}) \quad (28)$$

whereby in D we used $\det U_{\mu} = u_{\mu,0}^2 + u_{\mu,1}^2 + u_{\mu,2}^2 + u_{\mu,3}^2 = 1$.

Then the maximum of Eq. (24) is found when \mathbf{g} is set to the eigenvector of the matrix of Eq. (25) corresponding to the largest eigenvalue. The largest eigenvalue is $\lambda = \sqrt{D^2 + E^2 + F^2}$ and the corresponding eigenvector is

$$\left(D + \sqrt{D^2 + E^2 + F^2}, E, F \right)^T. \quad (29)$$

We refer the reader to [30] for more practical details related to the maximally Abelian gauge.

2.2.3. Overrelaxation

In order to reduce the *critical slowing down* of the relaxation algorithm on large lattices, the authors of [16] suggested to apply an overrelaxation algorithm which replaces the local gauge transformation $g(x)$ by $g^{\omega}(x)$, $\omega \in [1, 2)$ in each step of the iteration. In practice the exponentiation of the gauge transformation will be done to first order.

2.2.4. Microcanonical steps

Applying a gauge transformation $g^{\omega}(x)$ with $\omega = 2$ leaves the Landau/Coulomb gauge functional invariant but these so-called microcanonical steps have the beneficial property to lead to a faster decorrelation and thus to faster convergence of the functional from which the simulated annealing algorithm will profit.

2.2.5. Stochastic relaxation

The stochastic relaxation algorithm replaces the local gauge update $g(x)$ by a microcanonical step $g^2(x)$ with probability p and can lead to faster convergence on large lattices.

2.3. Simulated annealing

Annealing is a method in condensed matter physics to bring certain materials in their ground state by first heating them above their melting point and subsequently cooling them down very slowly. It is crucial hereby that the system is given enough time to thermalize at each temperature step. If so, the atoms will arrange themselves in such a way that the macroscopic system ends up in its – or at least close to its – lowest energy state.

The authors of [7] developed an analogy of annealing and mathematical optimization problems. Following this analogy, the function which is to be optimized corresponds to the energy of the solid and the optimum is the ground state.

The algorithm then simply performs local *Metropolis* updates where the acceptance probability of a random local gauge update $g(x)$ is given by

$$P[g(x)] = \begin{cases} 1 & \text{if } f^g(x) \geq f(x) \\ \exp\left(\frac{f^g(x)-f(x)}{T}\right) & \text{else.} \end{cases} \quad (30)$$

Thus, while in a hot temperature regime, the algorithm accepts a worsening of the local gauge functional with a non-vanishing probability which ensures that the algorithm may overcome local extrema in order to increase the probability to find the global optimum.

In practice, the Metropolis update gets replaced by *heatbath* updates that generate the new gauge transformation directly with the right Boltzmann like probability distribution.² In order to reach quicker thermalization at each temperature step, we perform three microcanonical steps after each change in temperature. Note that simulated annealing will never reach the required gauge precision θ very accurately, instead relaxation or overrelaxation which can be regarded as simulated annealing in the limit of zero temperature, should be run subsequently to fully reach the required precision. See also Sec. 6.4.

2.4. Putting things together

After we have listed the details of the underlying large scale optimization problem and the techniques to perform local optimizations, we are now in the position to consider the global optimization algorithm.

²We use the *Philox* RNG of the *Random123 library*[32] to generate random numbers in the heatbath kernel.

As mentioned before, due to the strict locality of the family of relaxation algorithms and the simulated annealing algorithm, we can perform a checkerboard decomposition of the lattice and operate on all sites of one of the two sublattices *even* and *odd*³ concurrently. All of the above mentioned algorithms have the same underlying structure which is depicted in Alg. 1.

Algorithm 1

```

while precision  $\theta$  not reached do
  for sublattice = even, odd do
    for all  $x$  of sublattice do
      for all SU(2) subgroups do
        local optimization: find  $g(x) \in \text{SU}(2)$  Step 1.
        which is a function of  $U_\mu(x), U_\mu(x - \hat{\mu})$ 
        for all  $\mu$  do
          apply  $g(x)$  to  $U_\mu(x), U_\mu(x - \hat{\mu})$  Step 2.
        end for
      end for
    end for
  end for
end while

```

We want to stress that the difference of the various update algorithms as well as the difference between the gauges under consideration lies exclusively in Step 1 whereas, as we list explicitly in Appendix A, the main work of the algorithm lies in Step 2 which is independent of the update type and of the target gauge.

3. CUDA

Here we briefly introduce the CUDA (Compute Unified Device Architecture) programming model and summarize the hardware properties of the GPUs we adopt in our study.

3.1. The programming model

The CUDA model demands the division of the underlying problem into subproblems, so-called *thread blocks*, that can be treated independently from

³The sum over the space-time indices $t+x+y+z$ determines whether a site is considered *even* or *odd*.

each other in parallel. These thread blocks, on the other hand, are ensembles of threads and the threads within a thread block may communicate with each other through shared memory. The independent thread blocks then form a so-called *grid*. This model is very flexible and allows the user to run a CUDA application on different hardwares (meaning different number of streaming multiprocessors (SMs) and CUDA cores) without the need for major adjustments.⁴ This abstraction layer is introduced into the C language by defining a new set of functions which are called *kernels* and are identified by the `__global__` declaration specifier. The kernel is executed N times where

$$N = \text{block size} \times \text{grid size} \quad (31)$$

and each kernel call is a thread in the nomenclature introduced above. For the invocation of the kernel a new syntax is introduced where the block size and the total number of blocks (grid size) is specified. A unique index is given to each thread to assign, e.g., different memory addresses to different threads.

A group of 32 threads (the number depends on the hardware generation) of the same block are tied together to what is called a *warp*. The operations of all threads within a warp are executed simultaneously as long as they follow the same instruction path. Otherwise, the operations become serialized resulting in up to 32 cycles instead of one, a *warp divergence* occurs.

To efficiently hide memory latencies it is inevitable to have many warps active at the same time on a SM. The possible number of active blocks (or warps) depends on the available hardware that has to be divided among the threads, e.g., it depends on how many registers and how much shared memory is needed for an individual kernel.

3.2. Memory Layout

In the CUDA terminology the CPU on which the CUDA application is run is called the *host*, whereas the GPU is called *device* and the associated memory is called host and device memory, respectively. Communication between host and device memory is the main bottleneck. Although, for many single GPU implementations, communication is only necessary in the beginning and in the end of an application. How one effectively can deal with

⁴Since we exclusively adopt devices of the Fermi generation, the characteristic of the SMs is always the same for our tests, see Sec. 3.3.

compute capability	2.0
cores / SM	32 per SM
warp size	32
L1 cache / SM	16 KiB or 48 KiB
shared memory / SM	16 KiB or 48 KiB
32-bit registers / SM	32768 (32Ki)
max. registers / thread	63

Table 1: Specifications of the Fermi architecture.

communication from device to device through the host memory in multi-GPU simulations is discussed in Sec. 5. The part of device memory that is accessible from the host as well as from all CUDA threads is called *global memory*. Global memory is allocated by a command in the host code. Each thread may then allocate its private *local memory* which resides in the same physical memory as global memory. Global and local memory are both cached in a L1 and L2 cache by default (for Fermi), on a cache miss the latency to device memory is very high. For most applications the bandwidth to device memory is another limiting factor, although it is large compared to a common CPU to RAM bandwidth.

For communication within a block *shared memory* can be used. Shared memory has a very low latency since it resides in the same hardware as the L1 cache.

3.3. Hardware

We adopt four different NVIDIA Fermi GPUs for our study, the GTX 480 and GTX 580 from the consumer section and moreover the Quadro 4000 and the Tesla C2070 from the scientific/HPC section. The Tesla C2070, opposed to the consumer cards, supports ECC (error correcting code) protection for DRAM. Recently, the successor of the Fermi architecture has been released (Kepler). In Tab. 1 we give the data which is common to all Fermi GPUs, the hardware details of the individual devices are summarized in Tab. 2.

4. Implementation details

4.1. Code design

The design goal of our code was the minimization of local memory usage. One of the main limiting factors of performance is the number of registers

	GTX 480	GTX 580	Quadro 4000	Tesla C2070
graphics clock	700 MHz	772 MHz	475 MHz	575 MHz
SMs	15	16	8	14
total CUDA cores	480	512	256	448
device memory	1.5 GiB	1.5 GiB	2 GiB	6 GiB
memory bandw.	177.4 GB/s	192.4 GB/s	89.6 GB/s	144 GB/s

Table 2: Hardware details of the Fermi devices that we adopt in this work.

that are available per thread: on Fermi GPUs, the latter bound is 63 registers of 32-bit each. If more variables (on the assembly level) are needed per thread, the registers are “spilled” to local memory. Local memory, as mentioned earlier, uses the same hardware as global memory and thus has the same (high) latency and bandwidth bounds. Besides register spilling another source of local memory usage may slow down the execution of a kernel: registers are not addressable and therefore will arrays generally be placed in local memory. In order to capacitate the compiler to place arrays in registers, the size of the arrays and all index variables that access elements need to be computable at compile time⁵. Early versions of our code fulfilled this requirement by manually unrolling all loops and using C macros to access array elements. The present code, however, uses template parameters for the lattice dimensions and the dimension N_c of the gauge group $SU(N_c)$. As a consequence, unrolling can perfectly be done by the compiler. This code design offers a very flexible setup for further lattice applications.

4.2. Reduce memory transfers

In order to reduce memory transfers between global memory and the kernel a 12 parameter representation of the $SU(3)$ matrices has been suggested [33, 18], i.e., only two rows of the matrix are stored and loaded. If we denote the first and the second row of the matrix with vectors \mathbf{u} and \mathbf{v} , respectively, then the third row is given by $(\mathbf{u} \times \mathbf{v})^*$. The extra numerical work to reconstruct the full matrix is hidden since our kernels are bound by memory transactions and not by floating point operations. This optimization reduces the number of bytes to load and store per site from 576 bytes to 384 in single precision.

⁵The latter statement implies that, for example, all for loops have to be unrolled.

4.2.1. Memory pattern

Due to the hardware design of NVIDIA GPUs one has to adopt special memory layouts to efficiently utilize the memory bus to global memory. The peculiarity of these devices is that memory transactions of threads of the same warp are coalesced if they reside in the same 128-byte aligned segment in global memory. Consequently, neighboring threads (i.e. neighboring sites) should access neighboring memory addresses to achieve high memory throughput. A natural memory layout where the gauge links (SU(3) matrices) are stored in one block in memory does not fulfill these requirements, hence the index order of the gauge fields in memory has to be adapted.

The authors of [28], e.g. use the native CUDA datatype *Float4* and therefore distribute the 12 real numbers of a SU(3) element (in the 12 parameter representation, see Sec. 4.2) to three *Float4* arrays. In contrast, we build on a more flexible way by employing one large float or double array, respectively, in combination with an access pattern class that hides the memory layout from the user. This strategy allows us to easily change the memory layout depending on the properties of the underlying application.

Here we list explicitly the memory patterns that are in use in our gauge fixing applications, whereby the slowest running index is listed first:

- *StandardPattern* (natural layout): t, x, y, z, μ, i, j, c
- *GpuPattern*: $\mu, i, j, c, p, [t, x, y, z]_p$
- *GpuPatternTimeslice*: $t, \mu, i, j, c, p, [x, y, z]_p$
- *GpuPatternParityPriority*: $p, \mu, i, j, c, [t, x, y, z]_p$
- *GpuPatternTimesliceParityPriority*: $t, p, \mu, i, j, c, [x, y, z]_p$

where $i, j \in \{0, 1, 2\}$ are the matrix indices, c identifies real ($c = 0$) and imaginary ($c = 1$) part of the complex number, $\mu \in \{0, \dots, 3\}$ is the direction of the link, t is the index in temporal direction and x, y, z correspond to the spatial components. The index $p \in \{0, 1\}$ stands for parity (*even* and *odd*, respectively) and in those patterns where it is in use the space-time indices are split into two groups

$$[t, x, y, z]_p := \{t, x, y, z \mid t + x + y + z \pmod{2} = p\} \quad (32)$$

and equivalently for $[x, y, z]_p$. Parity splitting is necessary to achieve coalesced access to global memory, since we operate on the parity even and odd sublattices separately (see Alg. 1).

The *GpuPattern* is used in the single GPU implementations of Landau and maximally Abelian gauge. For Coulomb gauge we employ the *GpuPatternTimeslice* for the global gauge field array and the *GpuPattern* in kernels that operate on $1 \times N_s^3$ sublattices, i.e., within a single time-slice. To reduce memory traffic between the nodes in the multi-GPU implementation we adopt the *GpuPatternTimesliceParityPriority*. This allows that only the active parity of the time-slices at the border can be transferred between nodes. All applications use the *StandardPattern* to read and write files with the natural ordering.

All patterns assume that the global array is allocated for full 18 parameter SU(3) links although the applications load and store only 12 parameters.

4.2.2. Representation of the SU(3) link variables

We define a template class *SU3* with a template parameter that determines the storage type. For matrices that reside in the global memory array we offer a class *Link* with three parameters: (1) the pointer to the global memory array, (2) a lattice site given in terms of an object of type *SiteIndex* and (3) the direction μ . No memory is allocated for *SU3<Link>* variables. For local matrices we offer the class *Matrix* which allocates local memory (or uses registers when possible) for matrix elements. Functions for copying between *SU3<Link>* and *SU3<Matrix>* are implemented, as well as functions to load only the first two rows (12 parameter representation) of the matrices as well as a function to restore the third row.

4.3. The eight-threads-per-site strategy

Within every iteration of the gauge fixing algorithms each site update needs its adjacent links. These are read from global memory and after the update they have to be written back to global memory. After having restored the third line, these eight SU(3) matrices per site equal 8×18 reals = 144 reals and therewith exceed the register limit of 63 per thread what results in register spills to global memory and as a consequence negatively effects the bandwidth bound performance of the kernel.

With the purpose of reducing register spills, we switch to a finer parallelization granularity: instead of assigning one thread to one lattice site we now tie eight threads to a single lattice site, i.e., one thread for each of the eight matrices that are involved in a site update. As a result, each thread needs only 18 registers to store the gauge link.

In order to avoid warp divergences the kernel is invoked with a thread block size of $8 \times 32 = 256$. By doing so, each of the eight warps takes care of one neighbor type of the 32 sites and thus all threads within one warp follow the same instruction path.

The gauge transformation is then accumulated in shared memory. Since one operates on the $SU(2)$ subgroups of $SU(3)$ and an $SU(2)$ matrix can conveniently be represented by four reals, this requires $4 \times 32 = 128$ reals or 512 bytes (SP) or 1024 bytes (DP) per thread block. To avoid race conditions on the shared array the accumulation is done using the *atomic_add* function in single precision and by explicit serialization using *__syncthreads()* in combination with *if*-statements in double precision⁶.

The benefit of this strategy is that, in single precision, no register spillings occur at all if no further constraints on the kernel are applied (see Sec. 4.4) and for double precision, register spills are drastically reduced. The drawback of the current implementation compared to a more conventional one-thread-per-site strategy is that the number of simultaneously computed sites per multiprocessors is decreased. Nevertheless this strategy results in a clear overall performance gain [27].

4.4. Optimizations

Besides the aforementioned algorithmic optimizations we further tuned our code by optimizing the CUDA settings.

First of all we set *launch bounds* to individual kernels: by specifying the number of threads per block and a minimum of active blocks a bound on the maximal register usage is given. Without *launch bounds* the compiler uses 45 registers in the overrelaxation kernel for Landau and Coulomb gauges, resulting in a theoretical occupancy of 42%. By setting the register limit to 32 the theoretical occupancy is increased to 67% on the cost of a small amount of register spilling (24 byte stack frame, 24 byte spill stores, 40 byte spill loads).⁷ The same settings are applied to the other gauge fixing kernels.

Fermi devices have a L1 cache that physically shares the same 64 KiB hardware (per SM) with shared memory. The size of the L1 cache and shared memory can be set by the user for each kernel. Since we only need 512 Byte

⁶*atomic_add* is not supported for datatype *double*.

⁷The given values for register usage and spilling are for CUDA Toolkit 5.0 compiled for compute capability 2.0. They vary between different between CUDA 4.x and 5.0 but the optimal launch bounds are found to be the same.

shared memory per block and a maximum of 4 blocks is possible, we only need a total of 2 KiB shared memory per SM. This allows us to set the kernel to a *prefer L1 cache* configuration which means 16 KiB shared memory and 48 KiB of L1 cache. With this setting the register spilling introduced by the launch bounds is cached more efficiently.

By a global compiler switch, the use of L1 cache can be set to either caching (default) or non-caching (`-Xptxas -dlcm=cg`) loads. By using non-caching loads our applications shows a small improvement in performance. This is due to the fact that the use of global memory is designed such that only in the beginning of each kernel the matrices are loaded to local memory (i.e., into registers) and after all operations are finished they are written back. In between there is no reuse of cached data and thus there is no benefit in caching at all. With non-caching load the L1 cache is solely used for register spilling and write-backs of register spills to the device memory are reduced or totally removed.

In all applications we compile with the *use_fast_math* switch. Single precision operations are then replaced by faster implementations on the expense of precision though we did not experience any effects by this setting. For double precision operations there is no such option.

4.5. Numerical accuracy

In the following we investigate the accumulation of numerical rounding errors within our lattice gauge fixing applications. A suitable measure is the conservation of unitarity of the SU(3) matrices during the progress of the algorithm through many iterations. In Fig. 1 we show

$$\frac{1}{4V} \sum_{\mu,x} |1 - \det(U_\mu(x))| \quad \text{and} \quad \max_{\mu,x} |1 - \det(U_\mu(x))| \quad (33)$$

from a run over 12000 iterations of the overrelaxation update on a 32^4 lattice in single (SP) and double (DP) floating point precision. Moreover the plot shows lines corresponding to a mixed precision (MP) ansatz which calculates the overrelaxation gauge update on the SP gauge fields in full DP (see Fig. A.11) while the less precision demanding application of the gauge transformation to the links (Step 2 in Alg. 1) is performed in SP.

In DP, both, the average and even the maximal value stay well below 10^{-12} whereas in SP the error accumulates to the order 10^{-3} . To overcome the loss of unitarity, one may use the unitarity as a constraint and thus reproject the links to SU(3) after a given number of iteration steps.

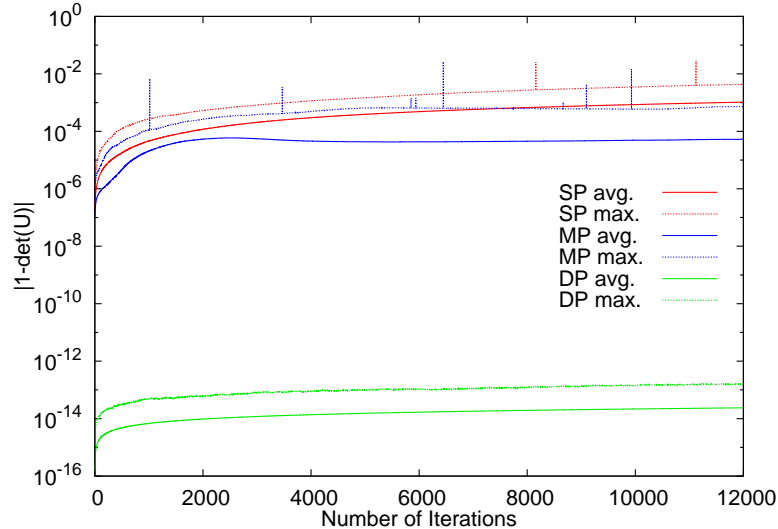


Figure 1: Conservation of unitarity ($|1 - \det(U)|$) in SP, MP and DP

The peaks in the SP maximum lines are individual outliers that occur approximately every 1000 iterations in one of the links of a 32^4 lattice on our GTX 580, whereas they could not be detected on the Quadro 4000.

Whether or not the loss of high precision unitarity in SP is of significance, depends of course on the individual problem the code is applied to. In Fig. 2 we show the value of the Landau gauge functional which is the sensitive quantity in our applications, in different precisions, again over 12000 iterations⁸ on a 32^4 lattice. It becomes obvious that SP without reprojection is not a good choice for lattice gauge fixing since the value of F^g even starts to decrease after around 3000 iterations. The DP functional value increases monotonically and finally reaches a plateau, this fact together with the previous mentioned maintenance of high precision unitarity lets us conclude that a DP simulation, even without reprojection, is very accurate. Thus, we can use the DP value as a benchmark for the other approaches. In the inner plot of Fig. 2 we show the relative deviation of each curve to the final DP result: SP with reprojecting to unitarity after every 100 steps and MP without reprojection stay within a relative deviation of 2×10^{-5} and MP with reprojection even within 5×10^{-6} . Moreover, the MP line shares the same qualitative behavior

⁸The gauge precision thereafter was $\theta < 6.0 \times 10^{-11}$ for the run in DP.

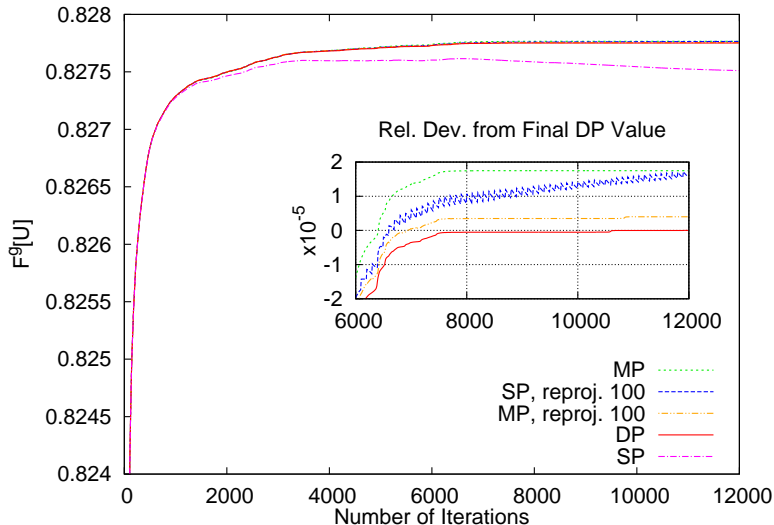


Figure 2: The value of the Landau gauge functional $F_{\text{Landau}}^g[U]$ as a function of the number of iterations of the overrelaxation kernel in single (SP), mixed (MP) and double precision (DP). In addition, the evolution of the functional value is shown when a reprojection to SU(3) is done every 100 iteration steps in SP and MP. The inner plot gives relative deviation of all curves (except SP without reprojection) from the final functional value in DP.

as the DP curve (monotonicity, convergence to a constant).

Therefore, our conclusion for the required floating point precision in lattice gauge fixing is as follows: in case one is primarily interested to actually fix the gauge of a gauge field configuration without being interested in the precise value of the resulting gauge functional, SP with reprojection is fine. If it is required to obtain the gauge functional value within a precision of no more than 10^{-5} , MP with reprojection is recommended since it retains most of the SP performance, as we will show in Sec. 6, opposed to DP which should only be chosen when one depends on a high precision result in the value of the gauge functional.

5. Multi-GPU

In the following discussion we will replace the space-time argument $x = (\mathbf{x}, t)$ by the time argument t alone wherever the \mathbf{x} dependence is of no significance in the given context. Moreover, we will assume that one MPI

process is assigned to one GPU device and thus use the terms process and device interchangeably.

In order to share the work which has to be performed locally on each lattice site, between several processes, we adopt a straightforward domain decomposition: we split the lattice of size $N_s^3 \times N_t$ into $N_t/nprocs$ partitions, where $nprocs$ denotes the number of processes involved in the parallelization. For Coulomb gauge this splitting is trivial since, as we discussed above, we can operate on the different time-slices separately and only need to apply the final gauge transformation $g(t)$ of the time-slice $U_\mu(t)$ to the temporal components of the preceding time-slice $U_0(t-1)$. This makes *on-the-fly* communication between devices for Coulomb gauge fixing unnecessary.

Manifestly covariant gauges like the Landau gauge and the maximally Abelian gauge, on the other hand, are more subtle. Here, all four neighboring links in the negative μ -direction have to be collected on each site x in order to calculate the gauge update $g(x)$ which subsequently is applied to all the eight links connected to the site x . Thus, with the ansatz of splitting the lattice across the temporal direction, we have to exchange the temporal components $U_0(x)$ of the gauge fields on time-slices that lie at the boundary of two processes.

5.1. Data exchange between neighboring devices

If we label the minimum time-slice that resides on a given device with t_{\min} and the maximum time-slice with t_{\max} , then only the calculation of the local gauge transformations $g(t_{\min})$ depends on the data exchange between different processes since for its calculation the gauge links $U_\mu(t_{\min}-1)$ that reside on the neighbor process are needed. Note that since we operate on the parity even and odd lattice sites consecutively, the currently active parity of the time-slice $U_\mu(t_{\max})$ is completely unaffected by the exchange with the neighboring process that only touches the passive parity part of $U_\mu(t_{\max})$. That means, on a given process, all time-slices except t_{\min} can be updated without exchanging any information with the neighbor processes. In order to update the $U_\mu(t_{\min})$ on all devices, however, the following set of instructions has to be carried out on each device in order to transfer the links $U_0(t_{\max})$ of device i to device $i+1$:

1. `cudaMemcpyDeviceToHost` of $U_0(t_{\max})$ (inactive parity)
2. `MPI_Send` of $U_0(t_{\max})$ to device $i+1$ and `MPI_Recv` of $U_0(t_{\min}-1)$ from device $i-1$

3. *cudaMemcpyHostToDevice* of $U_0(t_{\min} - 1)$
4. update $U_\mu(t_{\min})$ (active parity) which affects $U_0(t_{\min} - 1)$ (inactive)
5. *cudaMemcpyDeviceToHost* of $U_0(t_{\min} - 1)$ (inactive parity)
6. *MPI_Send* of $U_0(t_{\min} - 1)$ to device i and *MPI_Recv* of $U_0(t_{\max})$ from device $i + 1$
7. *cudaMemcpyHostToDevice* of $U_0(t_{\max})$

5.2. Data pattern

The memory pattern *GpuPatternTimesliceParityPriority*, introduced in Sec. 4.2.1, will be the pattern of choice for applications that get accelerated by a time-slice splitted multi-GPU approach. Not only is the time-index running slowest and thus allows to handle different time-slices separately in the latter mentioned pattern, moreover the time-slice internal pattern is very advantageous: each time-slice is split into its two parity parts of which each has the Dirac index μ running fastest, followed by the row index of the individual gauge matrices.

This layout ensures that the data which has to be exchanged, the first two rows (12 parameter representation) of the link variables $U_0(t_{\min})$ of a given parity, lie contiguous in device memory. The size of the data block that has to be exchanged is then given by the size of a time-slice multiplied by 1/2 (parity), 1/4 (Dirac index) and 2/3 (12 parameter representation), thus 1/12 in total.

5.3. Asynchronous memory transfers

We target at hiding the data exchange between different devices by overlapping them with calculations on the unaffected time-slices. Replacing the CUDA function *cudaMemcpy* with *cudaMemcpyAsync* results in a non blocking copying process from host to device or vice versa. Making use of different *cudaStreams* a device can then perform a copying request and execute a kernel at the same time.

In order to investigate how many time-slices are needed per device to fully hide the data exchange between two devices, we measured the time for the execution of the overrelaxation kernel on one time-slice and the time for a transfer of 1/12 of a time-slice for different spatial lattice sizes N_s^3 and averaged the result over 1000 iterations, see Tab. 3. As we can read off from the table, the asynchronous kernel execution on two time-slices takes longer then a device to host or host to device copy process, respectively. As

N_s^3	D2H [μs]	H2D [μs]	kernel [μs]	D2H/kernel	H2D/kernel
16	0.0398	0.0368	0.0209	1.90	1.76
32	0.2543	0.2276	0.1443	1.76	1.58
64	1.2510	1.1830	1.0489	1.19	1.13
128	8.9597	8.7169	8.3041	1.08	1.05

Table 3: The time needed to copy the relevant part (1/12) of a time-slice from device to host (D2H) and host to device (H2D) compared to the time needed to update one time-slice with the overrelaxation kernel (all in μs) averaged over 1000 iterations for different spatial volumes N_s^3 . The two most right columns give the ratios.

discussed above, the necessary data exchange between two devices includes in total four such copy processes and thus eight time-slices are enough to reach a complete overlap of data exchange from device to host (host to device) and calculations in the inner part of the domain.

So far we neglected the data exchange via MPI between the two neighboring host processes. As for the data exchange between host and device, here again it is advantageous to use non blocking functions for the data exchange, i.e., *MPI_Isend* and *MPI_Irecv*. By doing so we can again overlap the data exchange between the processes by calculations on time-slices that are not involved in the exchange.

In practice, we implemented the overlap of calculations with the data exchange between the processes and between host and device as a method of a communicator class. Then we only have to set up a certain update type (overrelaxation, simulated annealing etc.) and the *apply* method of the communicator object applies that update including full overlap with the data exchange.

6. Results

In this Section, we firstly examine the performance of the code on various devices including multiple GPUs. There, we pick the Landau gauge overrelaxation kernel as a representative for all kernels and gauges. Secondly, we outline a few sample results obtained by the application of our lattice gauge fixing code.

6.1. Performance on single GPUs

In Fig. 3 we show the performance of the overrelaxation kernel on the GTX 580 for different spatial volumes as a function of the temporal lattice

extent. The data stems from an average of one hundred repeated applications with 1000 iterations each. We achieve up to 370 GFlops in SP, up to 300 GFlops in MP and 80 GFlops in DP. The maximum performance of 370 GFlops corresponds to an execution time of 6.4s with the given lattice size and number of iterations. For the smaller lattices the theoretical occupancy of the device is not reached and therefore the maximum performance is not achieved. Apart from that, we find almost constant performance for all lattice volumes.

In Fig. 4 we compare the performance of different Fermi devices on lattices of size 32^4 . Our top performers in SP are the GTX 580 with nearly 370 GFlops, followed by the GTX 480 at around 300 GFlops. The difference between these devices results from the reduction in chip clock, number of SMs and bandwidth. The scientific GPUs are designed for a longer runtime and therefore the chip clock is remarkably lower. Thus, the performance of the C2070 is only close to 200 GFlops, the Quadro 4000 is at around 120 GFlops. Noteworthy is the difference between single and double precision: the theoretical ratio of SP to DP arithmetic operations for the scientific devices is 1:2, whereas the consumer GPUs have a ratio of 1:8. Accordingly, the performance ranking changes: still the GTX 580 performs best with approximately 80 GFlops, now followed by the C2070, slightly faster than the GTX 480 at around 70 GFlops. Thus, even for the scientific GPUs the theoretical factor of a half compared to SP could not be reached. The reason is that approximately twice as many registers are needed in DP and therefore even for the maximum of 63 registers *spilling* occurs. Additionally, the theoretical occupancy is reduced by the increase in registers.

The performance data given above is intended for comparing the algorithm on different architectures. It is based on counting Flops as described in Appendix A. The actual number of operations differs since we did not count the overhead for computing the third line reconstruction and we did not account for fused multiply-add operations. A true measure for the performance of our code is the number of instructions per cycle (IPC). For the top performer, the GTX 580, the IPC in SP is 1.49 which means roughly 75% of the peak performance, since a maximum of 2 instructions is issued per cycle. On the other hand, the global memory throughput is 120 GB/s which is only approximately 60% of peak. Combining these results, the most likely performance bound is not memory bandwidth, but *memory latency* which could theoretically be cured by increasing occupancy. In practice this is not possible, since this would mean further decreasing registers per thread

and thus introducing additional register spilling.

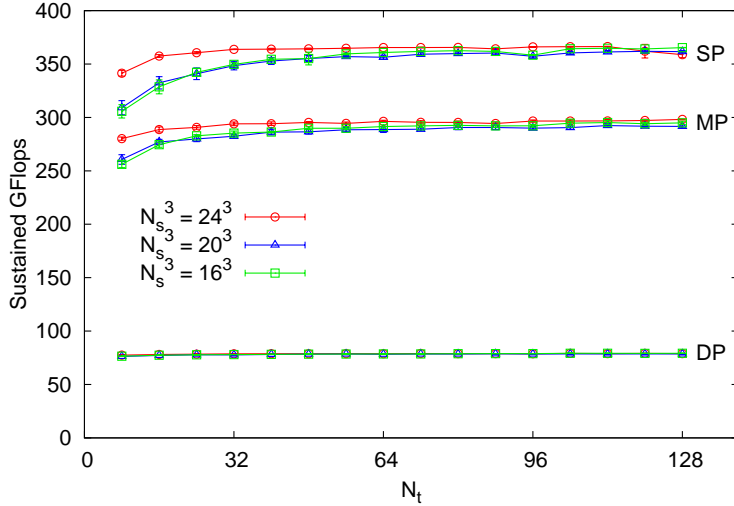


Figure 3: Performance of different spatial volumes as a function of the temporal lattice extend in SP, MP and DP on a GTX 580.

6.2. Performance on multi-GPUs

Our multi-GPU performance tests have been carried out on the “mephisto” cluster at the University of Graz. The cluster provides five compute nodes with four NVIDIA Tesla C2070 GPUs and CUDA 5.0. Moreover, each node offers two Intel Xeon Six-Core CPUs X5650 (“Westmere”) @ 2.67GHz on each node. The nodes are connected via InfiniBand and OpenMPI 1.4.3 and CUDA 5.0 is installed.

In the plot of Fig. 5 we show that linear weak scaling is reached with this strategy. The test have been performed on lattices of size $64^3 \times 32$ per GPU ($64^3 \times 512$ in total with 16 GPUs) and 48^4 per GPU ($48^3 \times 768$ in total with 16 GPUs). The higher performance of the spatial volume of 64^3 is simply due to higher occupancy: since we operate on single time-slices at a time, the lattice of spatial size 48^3 is not sufficient to efficiently occupy the device.

In Fig. 6 strong scaling is tested. For a total lattice size of $64^3 \times 256$ we find close to linear strong scaling up to 16 GPUs which corresponds to 16 time-slices per device. On a lattice of size $64^3 \times 128$ we find for 16 GPUs (eight time-slices per device) a performance loss of 15–30% (DP vs. SP). When

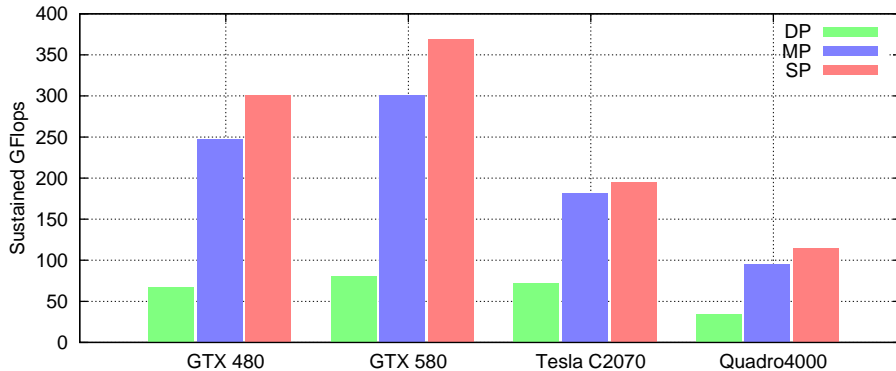


Figure 4: Performance of the Landau overrelaxation kernel on different NVIDIA devices in single (SP), mixed (MP) and double precision (DP) on a 32^4 lattice.

moving on to a smaller temporal lattice extent, $N_t = 96$, the performance decreases further. Moreover, for this lattice size, no gain in performance is apparent when adopting 16 instead of 12 devices.

6.3. Comparison to existing CPU code

Lastly, we compare our performance to the overrelaxation kernel of the *FermiQCD* library [34]. The *FermiQCD* toolbox is open source (C++) and has been designed to be easy to use while at the same time offering the user many applications for lattice QCD, in some applications at the expense of performance. To our knowledge, it is the only publicly available code that supports lattice gauge fixing with the overrelaxation algorithm in Landau gauge. We would be happy to compare our code to a wider range of implementations.

As test bed we chose an Intel Xeon Westmere CPU on the mephisto cluster, see Sec. 6.2. We run the *FermiQCD* Landau gauge overrelaxation kernel in SP on a lattice of size 32^4 on a single core in avoidance to reflect parallelization artifacts. Then we compare the performance to our code (same lattice size and precision) from the Tesla C2070 that the cluster offers.

FermiQCD reaches a performance of 0.414 GFlops and our code reaches for this setup 195.08 GFlops. Thus, our implementation executed on the Tesla GPU is equivalent to *FermiQCD* executed on ≈ 470 CPU cores of the given type, under the naive assumption of linear scaling for the CPU code.

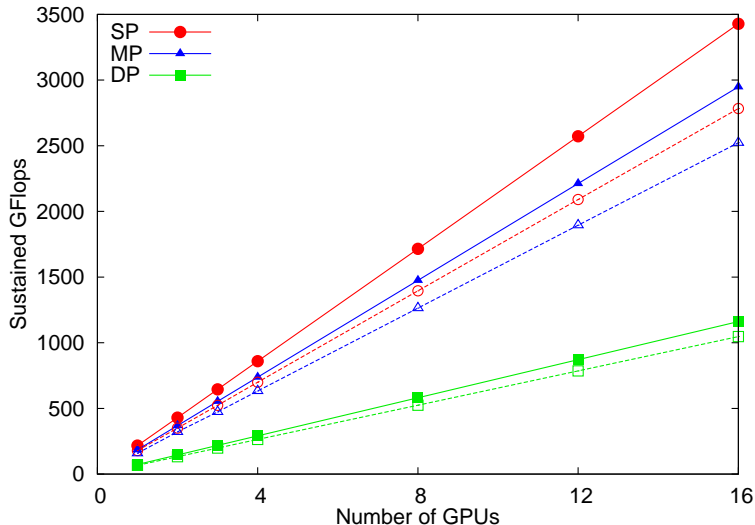


Figure 5: Weak scaling on the Tesla C2070 in single (SP), mixed (MP) and double precision (DP). The full symbols correspond to a lattice size of $64^3 \times 32$ per GPU and the open symbols to 48^4 per GPU.

6.4. Temperature dependence of the simulated annealing algorithm

In Sec. 2.3 we discussed the importance of keeping the temperature gradient small in the simulated annealing. Therefore, it is crucial to set up the right temperature interval in order not to waste many iteration steps in a temperature region where the gauge functional is insensitive to.

In Fig. 7 we show an example of the evolution of the gauge functional $F^g[U]$ and the gauge precision θ of the Landau gauge and the maximally Abelian gauge. The simulation has been performed on a *hot gauge field*, i.e., having all gauge links set to random SU(3) matrices. The lattice size is 32^4 and for both cases 10,000 simulated annealing steps have been carried out.

As one can read of from the plot, in this case, the sensitive region where the gauge functional changes most is for Landau gauge below $T < 4$ and for the maximally Abelian gauge slightly lower, $T < 2$.

6.5. Cooling down to maximally Abelian gauge

Here, we aim at reducing the time and number of iterations to gauge fix a configuration to the maximally Abelian gauge. We test overrelaxation versus a combination of simulated annealing, stochastic relaxation and overrelax-

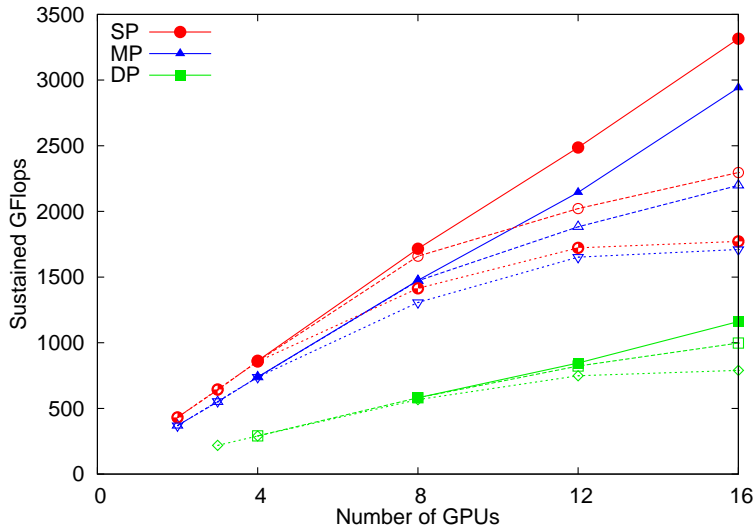


Figure 6: Strong scaling on the Tesla C2070. The spatial lattice volume is kept fixed at 64^3 and the total temporal extent varies for the three lines (per precision) from the top downwards $N_t = 256, 128, 96$.

ation in terms of required number of iterations to gauge fix a sample gauge configuration with inverse coupling $\beta = 5.7$ and lattice size 32^4 .

Both approaches use an overrelaxation parameter of $\omega = 1.35$, the second method starts off by applying 2000 simulated annealing steps including three microcanonical updates after each step (i.e., 8000 steps in total). Subsequently, a maximum of 2000 stochastic relaxation steps are applied and lastly overrelaxation until the precision $\theta < 10^{-12}$ is reached. Method one directly applies the overrelaxation kernel until convergence.

We started both variants on 100 randomly chosen points on the gauge orbit. Method one succeeded to find an optimum for 84 out of the 100 copies, the remaining 16 got stuck at a value of $\theta \approx 10^{-7}$ until the algorithm was stopped after one hundred thousand iterations. Method two was successful for 97 copies.

The average number of required iterations (the combined number of all updates) is given in Tab. 4, together with the final value of the gauge functional $F^g[U]$.

As it is evidence from the data, the combined approach of simulated annealing, stochastic relaxation and overrelaxation outperforms the pure overrelaxation method in terms of number of iterations by a factor of almost two

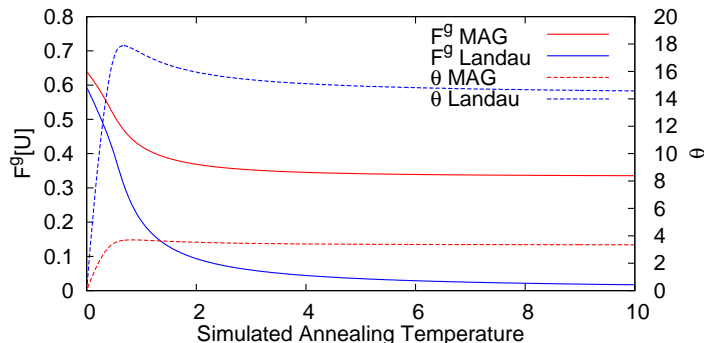


Figure 7: The temperature dependence in simulated annealing of the gauge functional $F^g[U]$ and the gauge precision θ of the Landau gauge and the maximally Abelian gauge.

	OR	SA/SR/OR
# of converged copies	83	97
# of iterations	272340 ± 8405	16701 ± 2562
$F^g[U]$	$0.74356431(39697)$	$0.74423815(10996)$

Table 4: Comparing the application of the overrelaxation algorithm (OR) solely, to the subsequent application of simulated annealing (SA) with microcanonical steps, stochastic relaxation (SR) and OR on 100 copies of a gauge field of lattice size 32^4 .

and moreover reaches an higher average value of the gauge functional while bringing more gauge copies to converge. The average time spend by the device (GTX 580) per gauge copy was four minutes for method two and slightly below seven minutes for method one. It has to be stressed, however, that not all gauge copies converged and hence these copies enter the average of the execution time with a biased weight since the kernel was executed until the maximum number of iterations was reached.

6.6. Towards the global maximum of the Landau gauge functional

We take the same gauge field configuration with $\beta = 5.7$ and lattice size 32^4 of the previous subsection and now aim at finding Landau gauge Gribov copies with gauge functional values as high as possible. Three runs with 100 random starts on the gauge orbit have been performed. The difference of the three runs lies in the number of simulated annealing steps that are applied before the overrelaxation kernel takes over. We apply zero, three thousand or ten thousand simulated annealing steps, respectively. The temperature

has been decreased from 4 down to 10^{-4} . Each simulated annealing step is followed by three microcanonical updates. Subsequently, we apply the overrelaxation kernel until $\theta < 10^{-10}$.

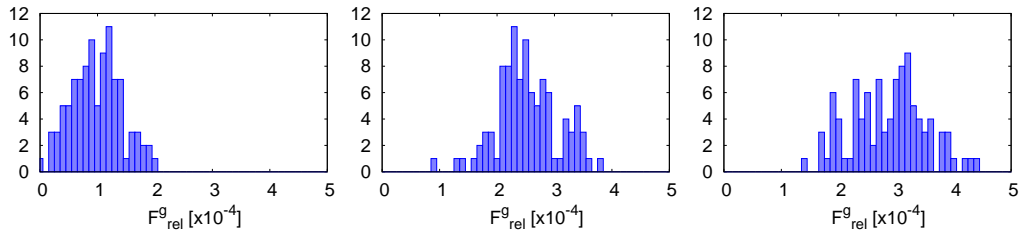


Figure 8: The relative deviation from the maximal gauge functional. From left to right with 10000, 3000 and zero simulated annealing steps.

We determined the maximum gauge functional value of all the runs, which we denote by F_{\max}^g and define the relative deviation from it by

$$F_{\text{rel}}^g = \frac{F_{\max}^g - F^g}{F_{\max}^g}. \quad (34)$$

The latter is plotted in histograms in Fig. 8 for all the three runs. The plot clearly demonstrates how the application of simulated annealing increases the chance to find the global maximum, especially on a relatively large lattice of size 32^4 . This test has been performed in parallel on two Tesla C2070 devices within several hours.

7. Summary

We presented a CUDA implementation for gauge fixing in lattice gauge field theories based on the relaxation algorithms. The code is based on the cuLGT package⁹ and supports the Landau, Coulomb and maximally Abelian gauge fixing conditions.

The implementation and the various optimization strategies have been discussed in detail. We showed that simulated annealing and overrelaxation can heavily be accelerated by employing GPUs. We listed convergence results in different floating point precisions and concluded that a mixed precision ansatz that performs only the critical parts of the simulation in double

⁹Both is available for downloaded under www.cuLGT.com.

precision is a good compromise in terms of precision ($\sim 10^{-5}$ relative to DP) and performance (80% – 90% of SP).

A maximum sustained performance of 370 GFlops on a single GTX 580 has been reached and moreover linear scaling on 16 Tesla cards with 3.5 Teraflops, given that the number of time-slices per device does not fall below 16.

Lastly, we demonstrated how the combination of simulated annealing and the various relaxation flavors can be tuned in such a way that either fast convergence to the gauge of choice is reached or alternatively that a gauge functional value as high as possible is obtained.

We are currently preparing tests on the Kepler architecture, updates on Kepler performance will be available on our homepage shortly.

Acknowledgments

We thank Giuseppe Burgio and Markus Quandt for helpful discussions and we are very grateful to Gundolf Haase and Manfred Liebmann for support with the “mephisto” cluster at the University of Graz. M.S. is supported by the Research Executive Agency (REA) of the European Union under Grant Agreement PITN-GA-2009-238353 (ITN STRONGnet).

Appendix A. Counting flops

As we discussed in Sec. 2.4, the main work of Alg. 1 consists of applying the new update $g(x)$ to the neighboring links of site x , i.e., Step 2 of the algorithm. We will now analyze this more quantitatively. In Fig. A.9 we show the code snippet of cuLGT for the multiplication of a SU(3) matrix with a SU(2) subgroup element from the left. Here, the SU(2) subgroup element is stored as a an object of class *Quaternion* (Cayley–Klein four parameter representation).

As we can read of from the figure, in the loop over k we encounter four complex multiplications (six flop each) plus two complex additions (two flop each), thus $28 \cdot 3 = 84$ flop for the update of $U_\mu(x)$ and equivalently for $U_\mu(x - \hat{\mu})$. Consequently, the number of flop for Step 2, in four dimensions, sums up to $84 \cdot 2 \cdot 4 = 672$ per lattice site and SU(2) subgroup and hence to $672 \cdot 3 = 2016$ for SU(3).

As mentioned before, the above part is the same for all gauges and all update types. Only Step 1 of Alg. 1 distinguishes between different gauges

and update types. Let us consider for example an overrelaxation update for Landau gauge. The latter consists of calculating $g(x)$ according to Eq. (19) plus a first order approximation of the exponentiation $g(x) \rightarrow g^\omega(x)$. In the cuLGT code, the sum of Eq. (19) is done on the *Quaternion* objects. Extracting the four reals of *Quaternion* representation of a SU(2) subgroup element of SU(3) requires four flop, see Fig. A.10. The *Quaternion* objects are then gathered in an array in shared memory (*shA*) according to Eq. (19). This means four flop (four additions) for each *Quaternion*. Thus the number of flop in Eq. (19) is eight per link variable and in 4D eight link variables are involved, i.e., 64 flop per lattice site and SU(2) subgroup iteration or 192 for SU(3).

Subsequently, the overrelaxation update $g(x) \rightarrow g^\omega(x)$ is calculated. Counting each operation in Fig. A.11 as one floating point operation (*rsqrt* corresponds to two operations), the *effective* number of flop for the overrelaxation update is 22 per lattice site and SU(2) subgroup, thus 66 for SU(3).

Summing up, the overrelaxation algorithm in SU(3) for Landau gauge requires

- 192 flop to gather the neighboring links $U_\mu(x)$, $U_\mu(x - \hat{\mu})$,
- 66 flop for the overrelaxation update,
- 2016 flop to apply the new $g(x)$ to $U_\mu(x)$, $U_\mu(x - \hat{\mu})$

and thus in total 2274 flop/site. Note that we do not take the extra Flops for the reconstruction of the third row of the SU(3) matrices into account.

For the heatbath kernel of the simulated annealing algorithm the number of flops cannot be calculated correctly because of the non-deterministic loops with random-number-dependent termination conditions. We counted the flops as if every loop is only run once and each RNG call is counted as one flop. Both choices are very conservative. Therefore, a comparison of simulated annealing implementations should be based on pure time measurements.

References

- [1] H. Neuberger, Nonperturbative BRs Invariance And The Gribov Problem, Phys.Lett. B183 (1987) 337.
doi:10.1016/0370-2693(87)90974-9.

- [2] L. von Smekal, D. Mehta, A. Sternbeck, A. G. Williams, Modified Lattice Landau Gauge, PoS LATTICE2007 (2007) 382. [arXiv:0710.2410](#).
- [3] L. von Smekal, A. Jorkowski, D. Mehta, A. Sternbeck, Lattice Landau gauge via Stereographic Projection, PoS CONFINEMENT8 (2008) 048. [arXiv:0812.2992](#).
- [4] S. Catterall, R. Galvez, A. Joseph, D. Mehta, On the sign problem in 2D lattice super Yang-Mills, JHEP 1201 (2012) 108. [arXiv:1112.3588](#), [doi:10.1007/JHEP01\(2012\)108](#).
- [5] D. Mehta, S. Catterall, R. Galvez, A. Joseph, Supersymmetric gauge theories on the lattice: Pfaffian phases and the Neuberger 0/0 problem, PoS LATTICE2011 (2011) 078. [arXiv:1112.5413](#).
- [6] D. Zwanziger, Renormalization in the Coulomb gauge and order parameter for confinement in QCD, Nucl.Phys. B518 (1998) 237–272. [doi:10.1016/S0550-3213\(98\)00031-5](#).
- [7] S. Kirkpatrick, C. D. Gelatt Jr., M. P. Vecchi, Optimization by Simulated Annealing, Science 330 (1983) 671.
- [8] G. Bali, V. Bornyakov, M. Müller-Preussker, K. Schilling, Dual superconductor scenario of confinement: A Systematic study of Gribov copy effects, Phys.Rev. D54 (1996) 2863–2875. [arXiv:hep-lat/9603012](#), [doi:10.1103/PhysRevD.54.2863](#).
- [9] D. Mehta, M. Kastner, Stationary point analysis of the one-dimensional lattice Landau gauge fixing functional, aka random phase XY Hamiltonian, Annals Phys. 326 (2011) 1425–1440. [arXiv:1010.5335](#), [doi:10.1016/j.aop.2010.12.016](#).
- [10] D. Mehta, A. Sternbeck, L. von Smekal, A. G. Williams, Lattice Landau Gauge and Algebraic Geometry, PoS QCD-TNT09 (2009) 025. [arXiv:0912.0450](#).
- [11] C. Hughes, D. Mehta, J.-I. Skullerud, Enumerating Gribov copies on the lattice, Annals Phys. 331 (2013) 188–215. [arXiv:1203.4847](#).

- [12] D. Mehta, Finding All the Stationary Points of a Potential Energy Landscape via Numerical Polynomial Homotopy Continuation Method, *Phys.Rev. E*84 (2011) 025702. [arXiv:1104.5497](#), [doi:10.1103/PhysRevE.84.025702](#).
- [13] D. Mehta, Numerical Polynomial Homotopy Continuation Method and String Vacua, *Adv.High Energy Phys.* 2011 (2011) 263937. [arXiv:1108.1201](#), [doi:10.1155/2011/263937](#).
- [14] D. Mehta, Y.-H. He, J. D. Hauenstein, Numerical Algebraic Geometry: A New Perspective on String and Gauge Theories, *JHEP* 1207 (2012) 018. [arXiv:1203.4235](#), [doi:10.1007/JHEP07\(2012\)018](#).
- [15] J. Mandula, M. Ogilvie, The Gluon Is Massive: A Lattice Calculation of the Gluon Propagator in the Landau Gauge, *Phys.Lett. B*185 (1987) 127–132. [doi:10.1016/0370-2693\(87\)91541-3](#).
- [16] J. E. Mandula, M. Ogilvie, Efficient gauge fixing via overrelaxation, *Phys.Lett. B*248 (1990) 156–158. [doi:10.1016/0370-2693\(90\)90031-Z](#).
- [17] P. de Forcrand, Multigrid techniques for quark propagator, *Nucl.Phys.Proc.Suppl.* 9 (1989) 516–520. [doi:10.1016/0920-5632\(89\)90153-9](#).
- [18] M. Clark, R. Babich, K. Barros, R. Brower, C. Rebbi, Solving Lattice QCD systems of equations using mixed precision solvers on GPUs, *Comput.Phys.Commun.* 181 (2010) 1517–1528. [arXiv:0911.3191](#), [doi:10.1016/j.cpc.2010.05.002](#).
- [19] R. Babich, M. A. Clark, B. Joo, Parallelizing the QUDA Library for Multi-GPU Calculations in Lattice Quantum Chromodynamics [arXiv:1011.0024](#).
- [20] R. Babich, M. Clark, B. Joo, G. Shi, R. Brower, et al., Scaling Lattice QCD beyond 100 GPUs [arXiv:1109.2935](#).
- [21] A. Alexandru, C. Pelissier, B. Gamari, F. Lee, Multi-mass solvers for lattice QCD on GPUs, *J.Comput.Phys.* 231 (2012) 1866–1878. [arXiv:1103.5103](#), [doi:10.1016/j.jcp.2011.11.003](#).

- [22] C. Bonati, G. Cossu, M. D’Elia, P. Incardona, QCD simulations with staggered fermions on GPUs, *Comput.Phys.Commun.* 183 (2012) 853–863. [arXiv:1106.5673](#), [doi:10.1016/j.cpc.2011.12.011](#).
- [23] A. Chakrabarty, P. Majumdar, Hybrid Monte Carlo with Wilson Dirac operator on the Fermi GPU [arXiv:1207.2223](#).
- [24] F. Winter, Gauge Field Generation on Large-Scale GPU-Enabled Systems, *PoS LATTICE2012* (2012) 185. [arXiv:1212.0785](#).
- [25] F. Winter, Accelerating QDP++/Chroma on GPU [arXiv:1111.5596](#).
- [26] M. Schröck, The chirally improved quark propagator and restoration of chiral symmetry, *Phys.Lett.* B711 (2012) 217–224. [arXiv:1112.5107](#), [doi:10.1016/j.physletb.2012.04.008](#).
- [27] M. Schröck, H. Vogt, Gauge fixing using overrelaxation and simulated annealing on GPUs, *PoS LATTICE2012* (2012) 187. [arXiv:1209.4008](#).
- [28] N. Cardoso, P. J. Silva, P. Bicudo, O. Oliveira, Landau Gauge Fixing on GPUs, *Comput.Phys.Commun.* 184 (2013) 124–129. [arXiv:1206.0675](#), [doi:10.1016/j.cpc.2012.09.007](#).
- [29] L. Giusti, M. Paciello, C. Parrinello, S. Petrarca, B. Taglienti, Problems on lattice gauge fixing, *Int.J.Mod.Phys.* A16 (2001) 3487–3534. [arXiv:hep-lat/0104012](#), [doi:10.1142/S0217751X01004281](#).
- [30] J. Stack, W. Tucker, R. Wensley, The maximal abelian gauge, monopoles, and vortices in SU(3) lattice gauge theory, *Nucl.Phys.* B639 (2002) 203–222. [doi:10.1016/S0550-3213\(02\)00537-0](#).
- [31] N. Cabibbo, E. Marinari, A New Method for Updating SU(N) Matrices in Computer Simulations of Gauge Theories, *Phys. Lett. B* 119 (1982) 387. [doi:10.1016/0370-2693\(82\)90696-7](#).
- [32] J. K. Salmon, M. A. Moraes, R. O. Dror, D. E. Shaw, Parallel random numbers: as easy as 1, 2, 3, in: *Proceedings of 2011 International Conference for High Performance Computing, Networking, Storage and Analysis, SC ’11*, ACM, New York, NY, USA, 2011, pp. 16:1–16:12. [doi:10.1145/2063384.2063405](#).

- [33] P. De Forcrand, D. Lellouch, C. Roiesnel, OPTIMIZING A LATTICE QCD SIMULATION PROGRAM, *J.Comput.Phys.* 59 (1985) 324–330. doi:10.1016/0021-9991(85)90149-4.
- [34] M. Di Pierro, et al., www.fermiqcd.net, *Nucl. Phys. Proc. Suppl.* 129 (2004) 832–834. arXiv:hep-lat/0311027.

```

template<class Type>
void SU3<Type>::leftSubgroupMult( lat_group_dim_t i,
                                lat_group_dim_t j, Quaternion<Real> *q )
{
    for( lat_group_dim_t k = 0; k < 3; k++ )
    {
        Complex<Real> IK = q->get( 0, 0 ) * get(i,k);
        IK += q->get( 0, 1 ) * get(j,k);

        Complex<Real> JK = q->get( 1, 0 ) * get(i,k);
        JK += q->get(1,1) * get(j,k);

        set( i, k , IK );
        set( j, k,  JK );
    }
}

```

Figure A.9: Multiplication of a SU(3) matrix by a SU(2) subgroup element in Quaternion representation from the left. The total number of flop is 84 per SU(2) subgroup iteration; see discussion in the text.

```

template<class Type>
Quaternion<Real> SU3<Type>::getSubgroupQuaternion(
    lat_group_dim_t iSub, lat_group_dim_t jSub )
{
    Quaternion<Real> q;
    Complex<Real> temp;
    temp = mat.get(iSub,iSub);
    q[0] = temp.x;
    q[3] = temp.y;
    temp = mat.get(jSub,jSub);
    q[0] += temp.x;
    q[3] -= temp.y;
    temp = mat.get(iSub,jSub);
    q[2] = temp.x;
    q[1] = temp.y;
    temp = mat.get(jSub,iSub);
    q[2] -= temp.x;
    q[1] += temp.y;

    return q;
}

```

Figure A.10: Extracting a SU(2) subgroup element of SU(3) in *Quaternion* representation.

```

void OrUpdate::calculateUpdate( volatile Real (&shA)[4*NSB],
                               short id )
{
    Real ai_sq = shA[id+NSB] * shA[id+NSB]
                +shA[id+2*NSB] * shA[id+2*NSB]
                +shA[id+3*NSB] * shA[id+3*NSB];

    Real a0_sq = shA[id] * shA[id];

    Real b = (orParameter*a0_sq + ai_sq)/(a0_sq + ai_sq);
    Real c = rsqrt( a0_sq + b*b*ai_sq );

    shA[id] *= c;
    shA[id+NSB] *= b*c;
    shA[id+2*NSB] *= b*c;
    shA[id+3*NSB] *= b*c;
}

```

Figure A.11: The overrelaxation update requires 22 flop per lattice site and SU(2) subgroup.